Supporting Information for:

Heating-Induced Transformations of Atmospheric Particles using Environmental Transmission Electron Microscopy

Daniel P. Veghte[1], Swarup China[1], Johannes Weis[2,3], Peng Lin[5], Mallory L. Hinks[4], Libor Kovarik[1], Sergey A. Nizkorodov[4], Mary K. Gilles[2], Alexander Laskin[5,]*

[1]William R. Wiley Environmental Molecular Sciences Laboratory, Pacific Northwest National Laboratory, Richland, Washington 99354, USA.
[2]Department of Chemistry, University of California, Berkeley, California 94720, USA.
[3]Chemical Sciences Division, Lawrence Berkeley National Laboratory, Berkeley, California 94720, USA.
[4]Department of Chemistry, University of California, Irvine, Irvine, California 92697, USA
[5]Department of Chemistry, Purdue University, West Lafayette, IN 47907-2084 USA.

*Correspondence: alaskin@purdue.edu

Particle Generation and Collection:

Sodium chloride (ACS reagent grade, >99+%, Aldrich, Inc.), ammonium sulfate (BioUltra, >99.5%, Sigma, Inc.), and SRFA (1S101F, International Humic Substance Society) were dissolved in ultrapure water at concentrations of approximately 1 wt. %. Particles were generated through nebulization of 1 mL of the corresponding solutions using a medical nebulizer (8900-7-50, Salter Labs, Inc.) with a nitrogen flow of 4 l min^{-1}. The particle stream was dried using a diffusion dryer (model 306200, TSI, Inc.). Dried particles were subsequently deposited onto microscopy substrates arranged on the 7^{th} stage (aerodynamic size range 0.32-0.56 µm) of a Micro-Orifice Uniform Deposit Impactor (MOUDI, model 110R, MSP, Inc.). The substrates included lacey carbon films on Molybdenum 300 mesh (Pacific Grid Tech, Inc.) and Aduro thermal E-chips with silicon carbide heating membrane with amorphous holey carbon (Protochips, Inc.). Powders of Glucose (99.5%, Sigma) and Tin (325 mesh, 99.8%, Alfa Aesar) were used as received. A small quantity of these powders was dispersed on the substrate surface and the excess particles were blown off by dry nitrogen. For experiments where particles were heated in the external tube furnace and subsequently analyzed by scanning transmission X-ray microscopy and near-edge X-ray absorption fine structure (STXM [1]/NEXAFS), the particles were deposited on silicon nitride membrane windows (Silson, Inc.). An additional set of samples with high particle loadings deposited on aluminum foils substrates (MSP, Inc.) was prepared for electrospray ionization-high resolution mass spectrometry (ESI-HRMS) analysis.

SOA were produced using a custom-built oxidation flow reactor (Figure S1). It consists of an 8 L quartz reaction vessel surrounded by nine 254 nm UV lamps inside a Rayonet RPR-100 photochemical reactor. To produce SOA, three separate air flows were combined inside the reaction vessel. The first flow contained ppm levels of ozone, which was produced by flowing dry air through an ozone generator lamp at a flow rate of 0.2 l min^{-1}. The second flow contained the VOC precursor vapor (p-xylene, toluene, or benzene). The VOC liquid was injected via syringe pump into a flow of dry air at a rate of 25 µL/hr. As the precursor was slowly pushed into the air flow, it evaporated and was carried into the main reaction vessel at a flow rate of 0.6 l min^{-1}. Finally, flowing dry air at a rate of 0.4 l min^{-1} through a Nafion drier (Perma Pure Inc.) humidified air inside the vessel. This resulted in a relative humidity of roughly 30% RH inside

the flow reactor. In the reactor, the ozone was converted, via reactions 1 and 2, into OH, which reacted with the injected VOC to produce SOA.

$$O_3 + h\nu \rightarrow O_2 + O(^1D) \quad \text{(R1)}$$

$$O(^1D) + H_2O \rightarrow 2\,OH \quad \text{(R2)}$$

$$OH + VOC \rightarrow products \quad \text{(R3)}$$

The steady state concentration of ozone was about 7.0 ppm inside the vessel with the UV lamps off. When the UV lamps were turned on to generate OH, the steady state concentration of ozone decreased to about 2.5 ppm. After generation, the SOA flowed out the exit tube and was collected onto microscopy substrates.

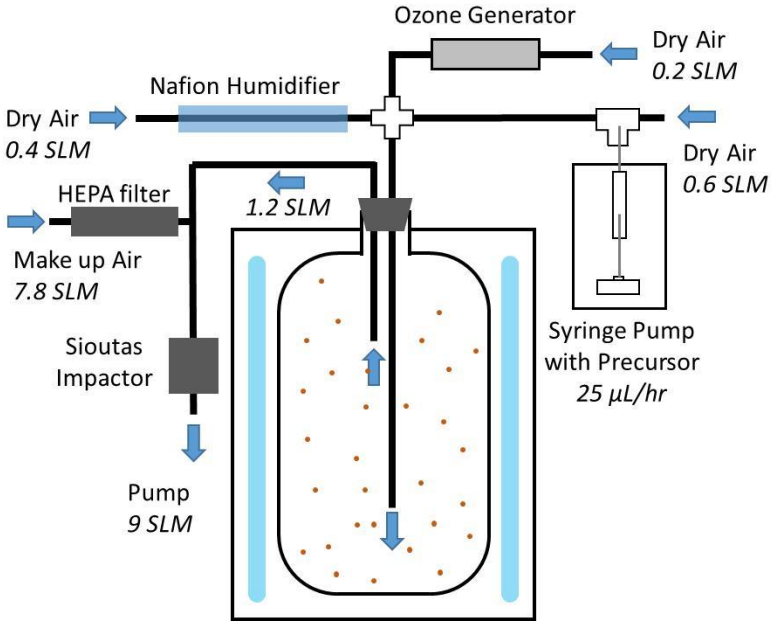

Figure S1. Diagram of the oxidation flow reactor for generation of the toluene, benzene, and p-xylene SOA.

Field samples of atmospheric particles were collected from 2/2/2014 (20:00) to 2/4/2014 (05:30) local time at the ZF2 site (2° 35' 21.1" N, 60° 6' 53.7") north of Manaus, Brazil.[2] Samples were collected on lacey carbon coated copper TEM grids on stage 8 of a MOUDI impactor (aerodynamic size range is 0.18-0.32 µm). The 72 hour back air trajectory was calculated using the Hybrid Single-Particle Lagrangian Integrated Trajectory (HYSPLIT) model (Figure S2).[3] The back trajectories show that the air parcel came from the Northeast and had little impact from urban anthropogenic sources.

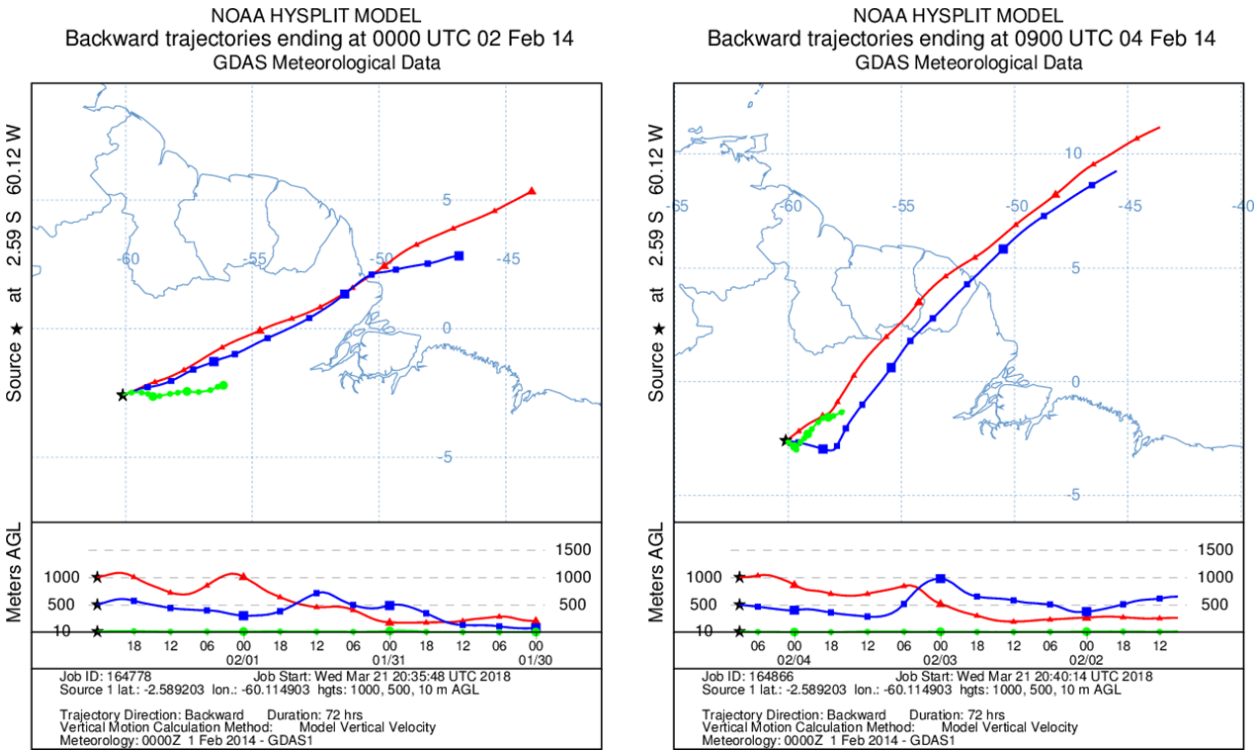

Figure S2. Hybrid Single-Particle Lagrangian Integrated Trajectory (HYSPLIT) back trajectories for the start and end times of the samples collected at the ZF2 site in Brazil.

Chemical Characterization Techniques:

Bulk samples of SRFA heated at a selected set of temperature settings were analyzed using an LTQ-Orbitrap™ ESI-HRMS (Thermo Fisher Scientific). Filter samples were extracted with 300 µL of solvent (water:methanol = 1:1). The extracts were filtered using syringe filters with 0.45 µm PTFE membrane to remove insoluble fractions. Acetic acid (1% v/v) was added to the solution prior to ESI-HRMS analysis to facilitate ionization efficiency. The instrument was calibrated with a standard mixture of caffeine, MRFA (L-methionyl-arginyl-phenylalanyl-alanine acetate·H_2O), and Ultramark 1621. The spray voltage was 4.0 kV, and the instrument was operated in positive ion mode. The MS scan range was *m/z* 100-2000 with a resolving power of 100,000 at *m/z* =400.[4-5]

STXM/NEXAFS was used to acquire the carbon (278-320 eV) and oxygen (525-550 eV) K-edge spectra of individual particles[6-8] before and after heating. The measurements were performed on beamlines 11.0.2.2 and 5.3.2.2 at the Advanced Light Source at Lawrence

Berkeley National Laboratory. Monochromatic incident photons from the light source were focused using Fresnel zone plates to spot sizes of 25-40 nm, depending upon the zone plate in use. Sets of raster scan images were acquired across particles at the selected X-ray energy, and the transmitted light was recorded. Spectra were reconstructed from single particles with a reference to the particle-free background regions.

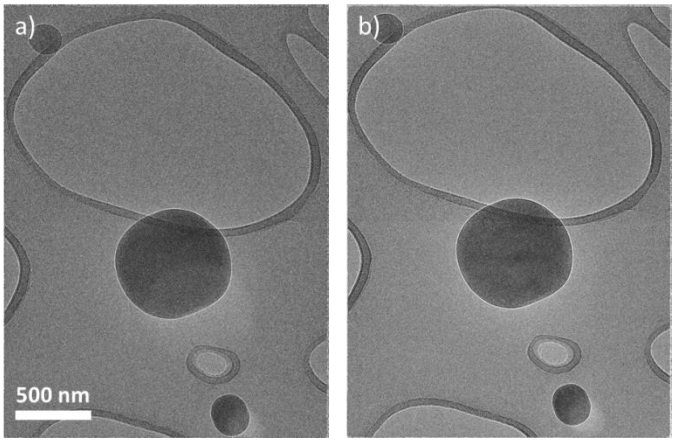

Figure S3. Low dose imaging of ammonium sulfate particles using the direct electron detector, a) initial and b) after 15 minutes of beam irradiation. No visual damage is observed in the images after beam irradiation.

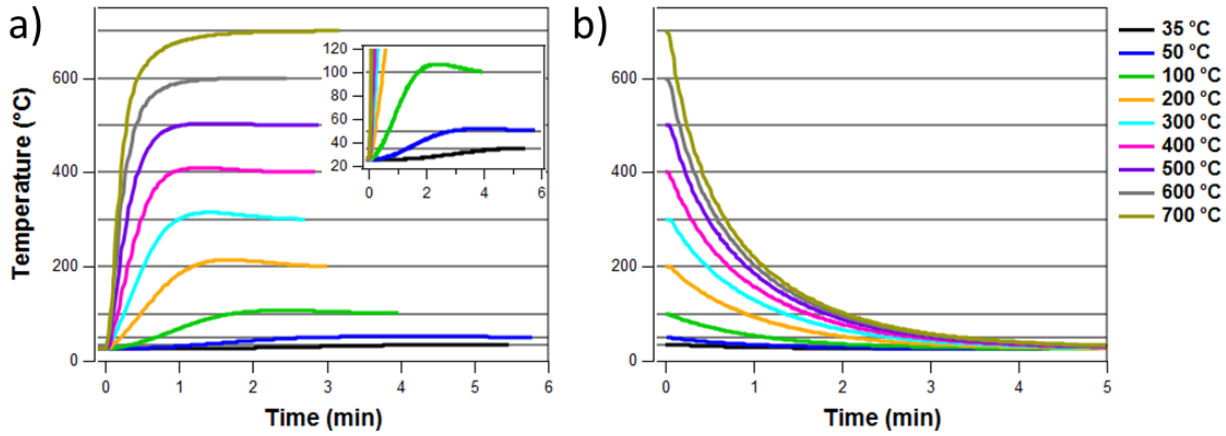

Figure S4. Temperature records showing the heating with inset expanding set points below 200 °C (a) and cooling (b) rates for each set point up to 700 °C in the furnace holder. Horizontal lines indicate the set point temperatures.

SEM images of particles impacted on the substrate (Figure S5) demonstrate that laboratory generated SOA have substantially lower viscosities than SRFA particles at ambient

temperature and humidity. SOA particles exhibit an oblate spheroid (flattened) morphology, suggestive of a liquid-like viscosity (<10 Pa s), while SRFA particles appear as spherical 'billiard ball' shapes, indicative glass-like high viscosities (>10^9 Pa s) under ambient temperature and humidity.[9] At low humidity (<20%) toluene SOA is expected to have a glass-like viscosity (>10^9 Pa s).[10] Experiments were performed to probe the volatility of SOA particles compared to the more viscous SRFA particles. In these experiments, continuous carbon film TEM substrates could not be used for SOA particles because their flattened morphology led to no discernable differences in mass loss during heating experiments. Instead, SOA particles were deposited on lacey carbon film TEM substrates. In these samples, SOA particles form a bead around individual thin strands of the lacey film and changes in particle volume (Figure S6) can be observed. Over the course of the heating experiments both the length and thickness of the particles adhered to the substrate change. Since lacey film substrates are not available with the MEMS device, only the furnace heating experiments were feasible.

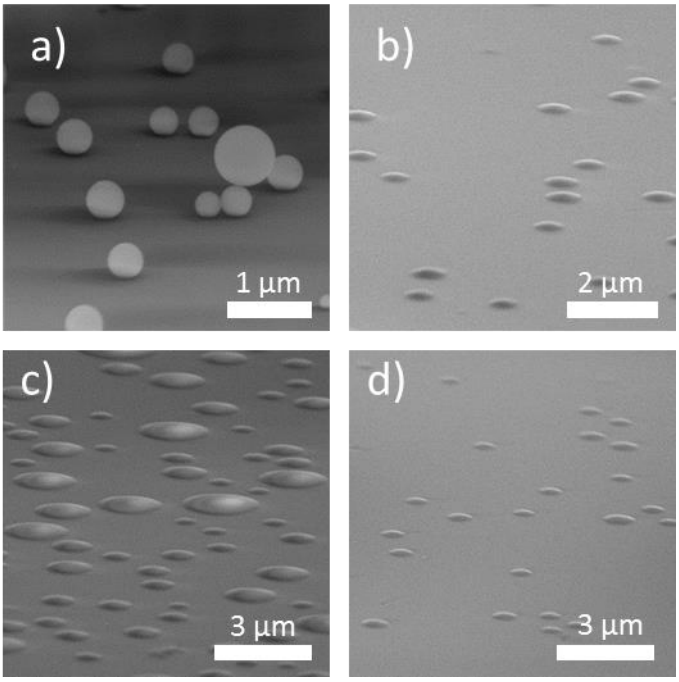

Figure S5. SEM micrographs taken at 75° tilt angle: a) SRFA, b) *ben*-SOA, c) *xyl*-SOA, and d) *tol*-SOA particles impacted onto TEM grids with a continuous carbon film.

For spherical and irregularly shaped particles (AS, glucose, and SRFA), particle size were calculated as equivalent circle diameters of the projected area. Obtained diameters were then used to calculate particle volume, assuming they were spheres. For NaCl particles, which are approximately cubic, the projected area was treated as an equivalent square and the calculated side length of the square was used to calculate its volume as a cube. For low viscosity particles (i.e. SOA), the calculated volume was based on the measured height and length of each side of the SOA material beaded up around individual thin strands of the lacey carbon film. The measured height and width were used to fit a Gaussian distribution to each side of the SOA particle excluding the carbon film (Figure S6). The volume integral of the fitted function was then used to approximate the particle volume.

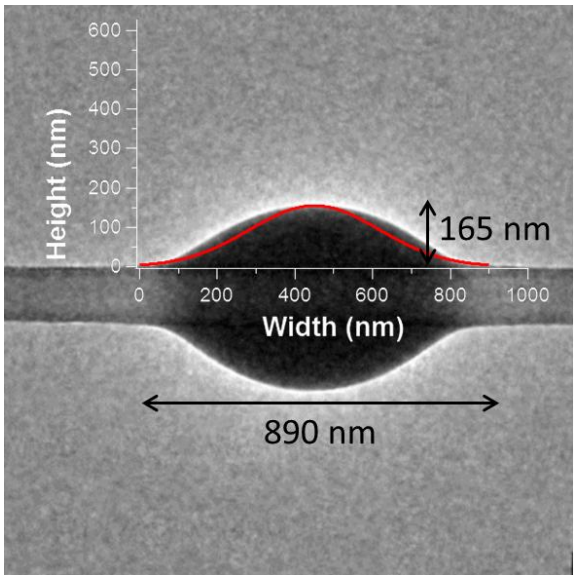

Figure S6. Diagram showing the overlay of the Gaussian fit (red line) to a toluene SOA particle adhered to the thin strand of the substrate. The volume integral of the function is then used to estimate the volume of the particle excluding the substrate.

Heating Holder Calibration:

Glucose, AS, tin, and NaCl particles were used to compare the set temperature conditions of the two heating holders. For glucose in the furnace holder no morphological changes were observed until the holder reached a set point of 110 °C. At this set temperature a small amount of sublimation of the material (Figure S7) was observed. When the particles were heated to a set point 120 °C, almost complete removal of the particles was observed. Some residual remained

that did not change upon further heating. Heating glucose with the MEMS holder showed changes at higher set temperatures; sublimation began at 150 °C and most material was completely removed by 160 °C. The vapor pressure of glucose is 2.6×10^{-5} mbar at 122 °C,[11] an order of magnitude higher than the vacuum level used in the ETEM for the calibration experiments. This indicates that the glucose particles will sublime at temperatures below 122 °C under high vacuum conditions. This suggests that the furnace holder is well calibrated up to ~100 °C since the particles were completely removed by 120 °C while the MEMS required heating up to a set temperature of 160 °C for the same response, a difference of approximately 40 °C. This result shows that the furnace holder is more accurate at lower temperatures.

Sublimation of AS during heating experiments in the ETEM is shown in Figure S7. As noted above, no visible beam damage on AS was observed using low dose imaging after 15 minutes of electron beam exposure (Figure S3). Initially, AS particles were nearly spherical in morphology. The first change in their morphology was seen at a set temperature of 80 °C in the furnace holder, where the particles began to adhere to the lacey film. By a set point of 100 °C there was substantial loss of AS, and by 120 °C only a small residual remains. In the MEMS experiment, the initial particle changes were observed at a set temperature of 120 °C where particles began to deform. Substantial loss of material was observed at the 160 °C set point, and by 180 °C only residuals of the AS particles remained. Heating to higher temperatures had no effect on the particle residuals with either holder type. The initial morphological changes and complete particle removal occurred consistently at a lower set temperatures (by 40-60 °C) in the furnace holder than in the MEMS heater. This trend between the furnace and MEMS holder temperatures is similar to that observed in glucose experiments where sublimation occurred at a higher set temperature in the MEMS than in the furnace holder. Previously, the volatility of AS has been previously studied using thermal denuder (TD) and thermal gravimetric (TG) methods. Using TG the release of ammonia and subsequent formation of bisulfate was seen at 100 °C.[12] Additionally, considerable volume loss of AS was observed in a range of 150-200 °C.[12] Independent TD studies with AS have shown complete evaporation occurring between 150 °C [13] and 180 °C.[14] Although the TG and TD analyses are consistent with the MEMS results reported here, the effect of high vacuum will lower the sublimation point of the AS, demonstrating again that the furnace holder is more accurate at lower temperatures.

The melting point of tin (230 °C) was used as an additional calibration point. The behavior of tin in the furnace holder and MEMS device was similar, melting between 220 °C and 230 °C. Melting was indicated by an abrupt change from irregularly shaped particles to spherical shapes (Figure S7), consistent with previous microscopy measurements.[15] The temperatures for melting observed in the furnace holder and MEMS device are consistent with the known melting point of tin of 232 °C.[16] These experiments demonstrate that at around 230 °C both holders are in agreement and well calibrated.

ETEM images in Figure S7 compare the heating of NaCl particles in the furnace holder and the MEMS device. Initially, NaCl particles were cubic-like with rounded edges. In a previous FTIR spectroscopy study, a trace amount of water was observed in NaCl particles dried to <10% RH, suggesting that trapped water is common in NaCl particles.[17] Trapped water changes the particle structure and leads to incomplete crystallization of NaCl forming non-perfect cubic structures. In heating experiments, the first changes in NaCl morphology were observed at the set temperatures of 480 °C and 400 °C for the furnace holder and the MEMS device, respectively. Under these conditions, the crystals transform and their edges sharpen, indicating the loss of trapped water and recrystallization. Heating NaCl powder using differential thermal analysis showed a phase change at 400 °C,[18] consistent with the changes measured in the MEMS experiment. For the furnace experiment, full dehydration and crystallization of NaCl particles is observed at a set point of 510 °C, followed by complete sublimation at 570 °C. Similarly, the MEMS results showed complete crystallization of the NaCl particles at a set point of 420 °C, subsequent loss of particles at 440 °C, and only residuals remain after further heating. The vapor pressure of NaCl is approximately 10^{-5} mbar at 485 °C[19] (higher than 10^{-6} mbar pressure in the ETEM under high vacuum) indicating that sublimation is the removal mechanism for NaCl particles. In contrast, thermal methods at ambient pressure do not show any mass loss in NaCl particles until >700 °C where the temperature approaches the melting point of NaCl of 801 °C.[18] At temperatures above ~400 °C, the set temperatures required for similar particle changes are 80-110 °C higher for the furnace holder than for the MEMS device. At these higher temperatures (>400 °C), substantial heat loss from the heating ring in the furnace holder occurs, resulting in a lower substrate temperature than measured by the thermocouple on the holder. Inherent to the technical design of a heating element embedded in the substrate itself, the MEMS

device is less affected by these issues and the changes in NaCl morphology occur over a narrower range of the set temperatures (400-440 °C) than in the furnace heating holder (480-570 °C). The volume fractions remaining for glucose, AS, and NaCl along with the roundness of tin particles in the furnace and MEMS experiments were measured and their values compared as shown in the supplemental information (Figure S8). We conclude that the MEMS device is robust and phase changes occurred at temperatures similar to the literature reported values, while the furnace holder required higher temperature to observe the same changes.

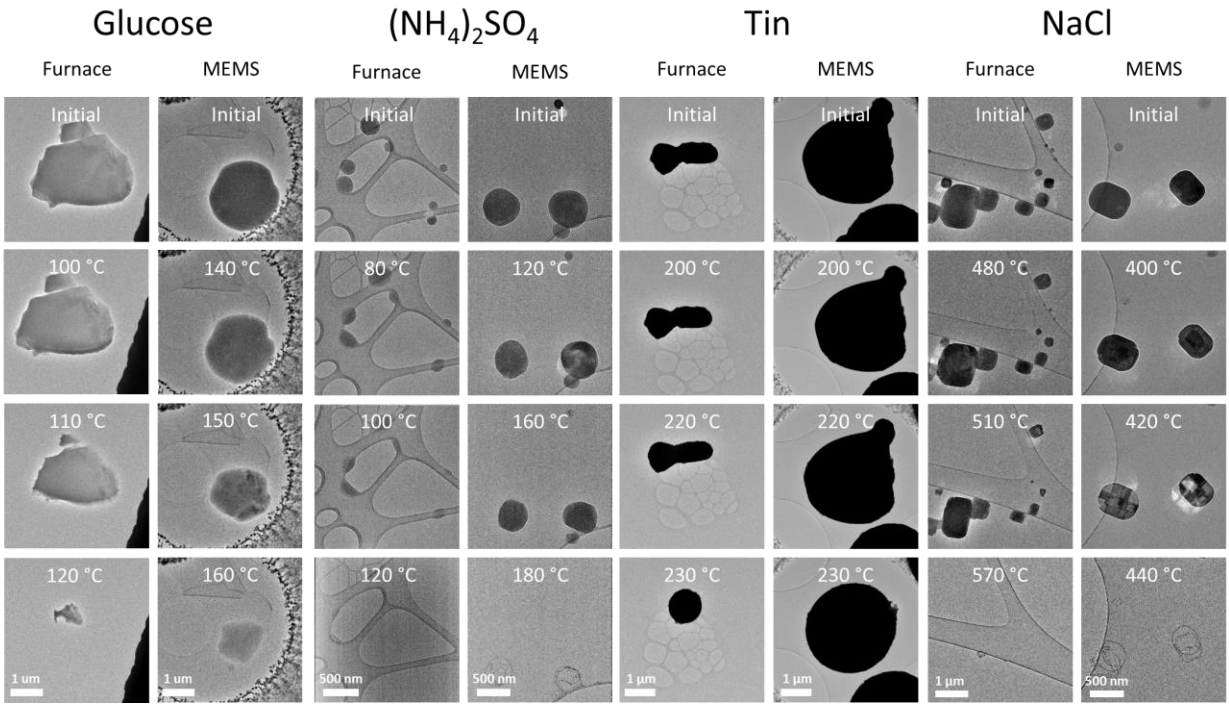

Figure S7: ETEM images of glucose, $(NH_4)_2SO_4$ or ammonium sulfate (AS), Tin, and NaCl particles heated using the furnace holder and MEMS device. Glucose is shown from the initial particles through the initial changes and to complete sublimation of the particles with only residuals remaining. Note the small particles on the edge are part of the SiC substrate. Transformations of AS are shown before and after heating at temperature corresponding to initial conditions at room temperature first discernable changes of particle morphology, intermediate stage, and complete removal of particles. Transformations of tin particles shown at the beginning of the experiment, at temperatures below the melting point, where no differences in shape are observed, and above the melting point. Transformations of NaCl particles are shown from initial morphologies, followed by the first noted discernable difference, complete dehydration and complete sublimation.

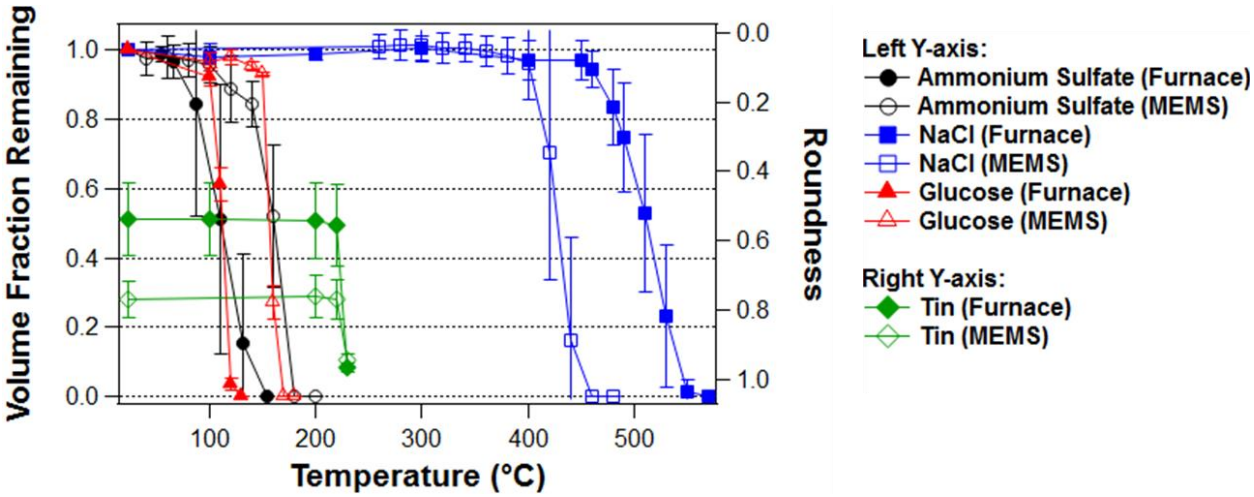

Figure S8: Comparison of the volume fraction remaining of glucose, ammonium sulfate and NaCl particle along with the roundness of tin using the furnace and MEMS heaters. Note that for the roundness parameter, further from 1 (perfect circle) indicates deviance from roundness. The initial roundness is indicative of the starting particle morphology and varies between particles and only the change should be noted for each experiment type. Error bars represent the standard error of the measurements.

Low volatility SRFA particles served as an additional standard to further delineate the differences between the set and real sample temperatures for the furnace holder. In these measurements, SRFA particles were heated up to a temperature set point of 800 °C in the furnace holder and up to 1100 °C in the MEMS. Complete evaporation of the SRFA particles is not expected until above 4000 °C where sublimation of elemental carbon occurs.[20] Figure S9a-h compares ETEM images of spherical SRFA particles at increasing temperatures. During the heating experiments, the SRFA particles shrink through volatilization and remain nearly spherical, exhibiting no visual deformation or adhesion to the substrate. To confirm that the particles retained spherical morphology after heating, SEM imaging of tilted SRFA samples was performed indicating no changes in particle shape occurred (Figure S10).

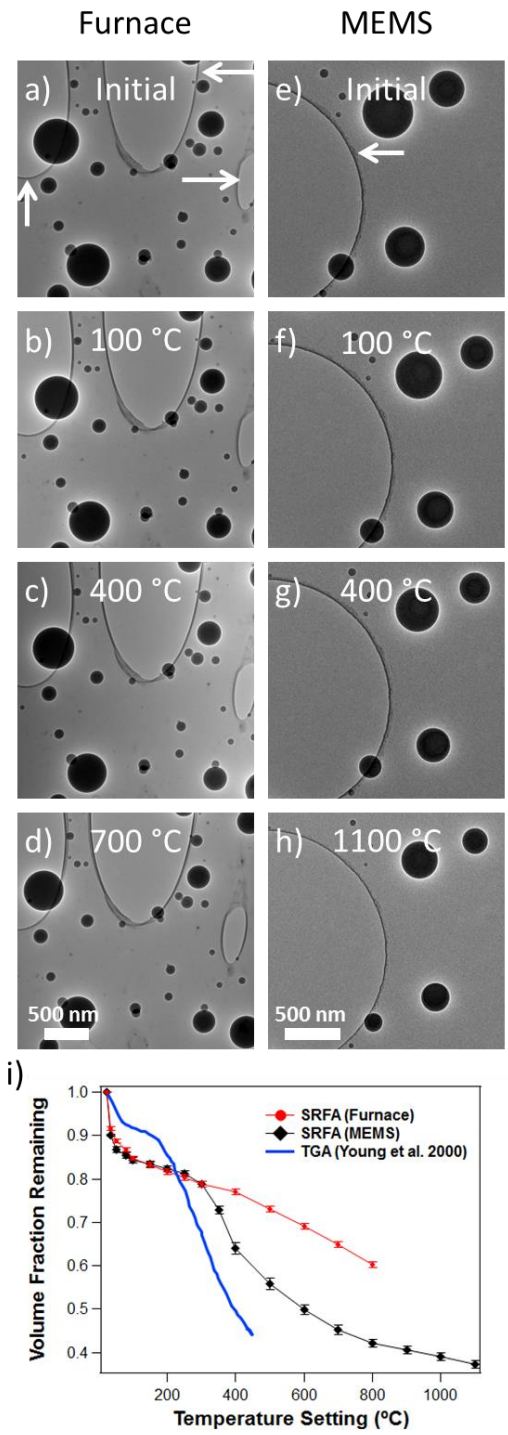

Figure S9: (a-h) ETEM images of SRFA particles heated using the furnace holder and MEMS device. The arrows indicate the edge of the carbon film where holes are present. Particles on edges of the carbon film do not adhere or change shape with increasing temperature. (i) Volume fraction remaining of SRFA particles as a function of temperature for the furnace holder and the MEMS device compared to bulk thermogravimentric analysis previously reported.[21] Error bars correspond to the standard error.

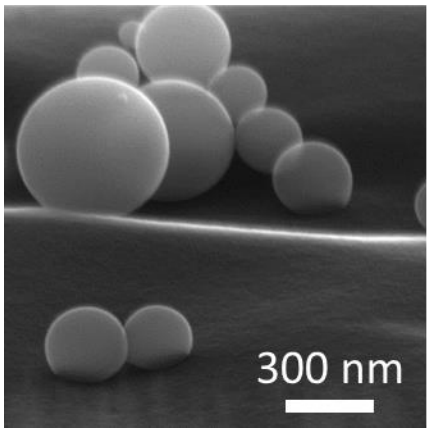

Figure S10. SEM micrograph of SRFA particles on the MEMS substrate at a tilt angle of 75° after being heated to 1100 °C in the TEM.

Calculated volumes of SRFA particles heated to selected set temperatures were additionally used to validate the furnace holder measurements against the MEMS observations. The changes in volume of the SRFA particles are shown in Figure S9 as a function of the set temperature during heating experiments using the furnace holder and the MEMS device. In both experiments, below 100 °C there is a substantial initial volume loss and approximately 85% of the original particle volume remains. In the 100-300 °C range, there is an additional decrease of about 5% with approximately 80% of the original particle volume remaining. These volume losses are roughly similar to those reported by Nie et al. for HULIS particles where 55-70% of the particle volume remained after heating to 280 °C using a thermal denuder.[14] In the furnace holder experiments, the steady decrease in particle volume continues up to 800 °C, where approximately 60% of the original volume remains. In the MEMS experiments, a sharp decrease in the particle volume starts at 350 °C and levels off at about 40% at 1000 °C. Heating above 400 °C leads to charring of the organic components, while complete loss of char can only be obtained either at 850 °C in the presence of oxygen[22] or by sublimation of charred carbon at 4000 °C.[20] Previous studies showed that when SRFA was heated during thermal gravimetric analysis (TGA), there was a sharp mass loss of approximately 8% by 100 °C. The mass loss then plateaued until approximately 200 °C. At ~200 °C a sharp decrease in the mass occurred and only 40% of the initial mass remained at 450 °C.[21] The TGA data are similar to the MEMS data reported here, demonstrating close agreement between set and reported temperature for the

sample in the MEMS device. The difference in the temperatures where the particles start to dramatically lose volume between MEMS and TGA experiments can be attributed to MEMS being under high vacuum, while TGA measurements were performed under ambient conditions (Figure S9). Additionally, Figures S11 and S12 shows the heating of SRFA with 1 mbar of N_2 and a mixture of 80:20 N_2:O_2 using the furnace holder. Heating with a pressure of 1 mbar compared to 10^{-6} mbar under an inert atmosphere shows that there is more removal of material from the particles under high vacuum conditions. When O_2 is introduced into the system, there is an additional increase in particle volume loss at temperatures above 250 °C. Additional experiments would need to be performed to further quantify these phenomena since the introduction of a gas will lead to additional heat losses and a lower temperature on the substrate. The change in particle size with increasing temperature shows that SRFA can be used as a validation standard due to the steady loss of material.

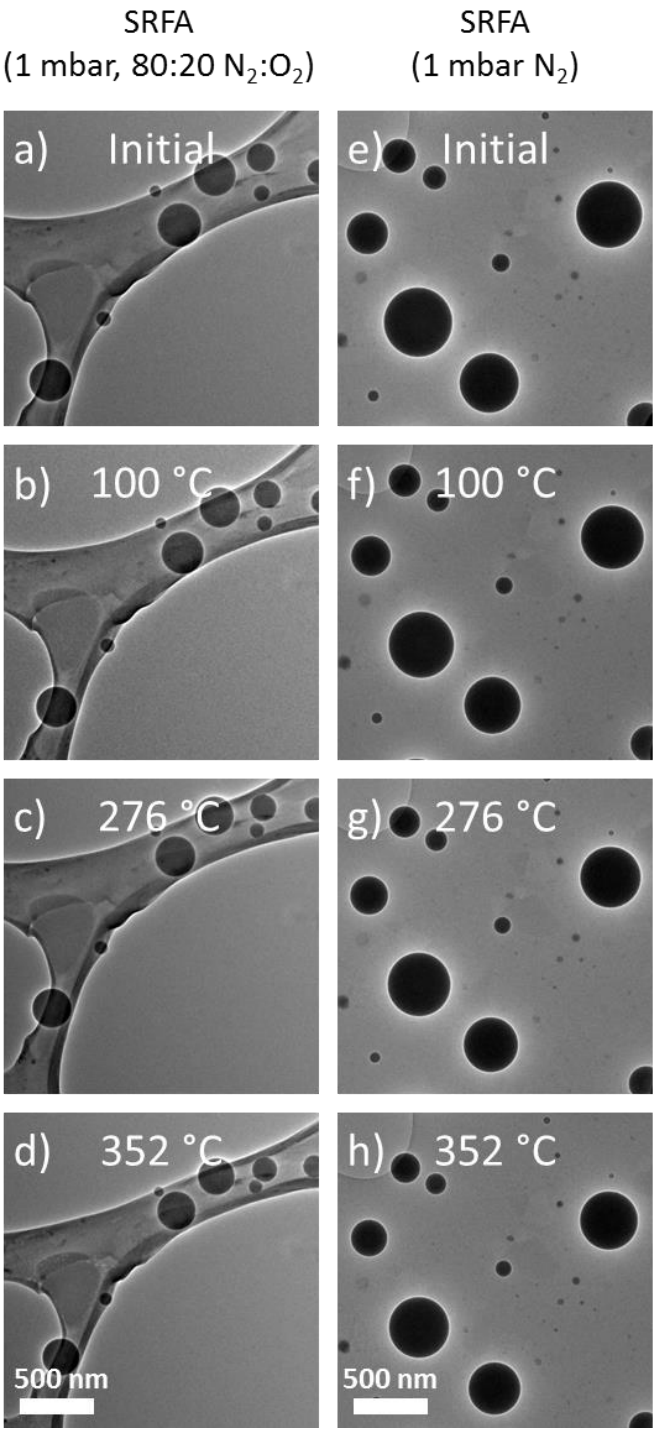

Figure S11. Images of SRFA particles heated under at 1 mbar of N_2 and 80:20 N_2:O_2 for temperatures up to 352 °C in the corrected furnace holder.

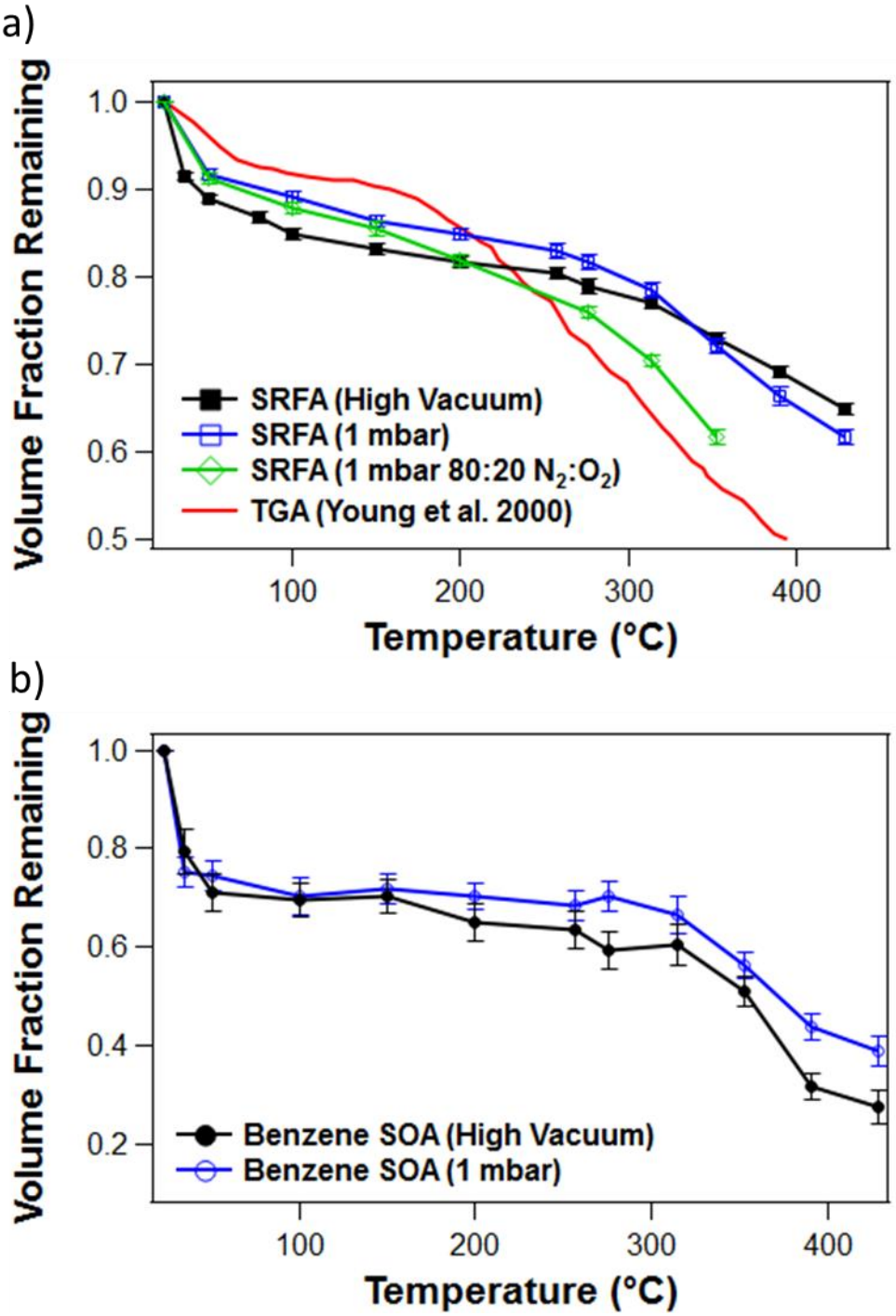

Figure S12. Volume fractions remaining of a) SRFA and b) *ben*-SOA particles heated at high vacuum (10^{-6} mbar) and 1 mbar N_2 using the corrected furnace heating holder temperatures. Additionally, the volume fraction remaining of SRFA particles are shown for an experiment under 80:20 mixture of N_2:O_2. The volume fraction remaining decreases substantially above 300 °C for SRFA particles heated under an oxygen rich atmosphere compared to a pure nitrogen atmosphere. Error bars represent the standard error.

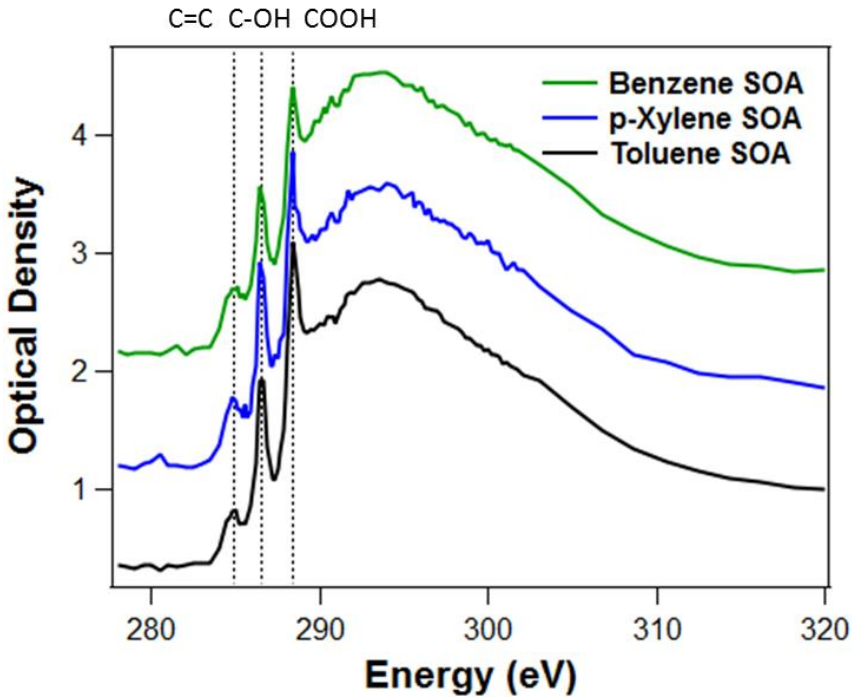

Figure S13. STXM/NEXAFS carbon K-edge spectra of laboratory generated *ben*-SOA, *xyl*-SOA, and *tol*-SOA particles. The spectra are normalized to the post edge and offset for clarity.

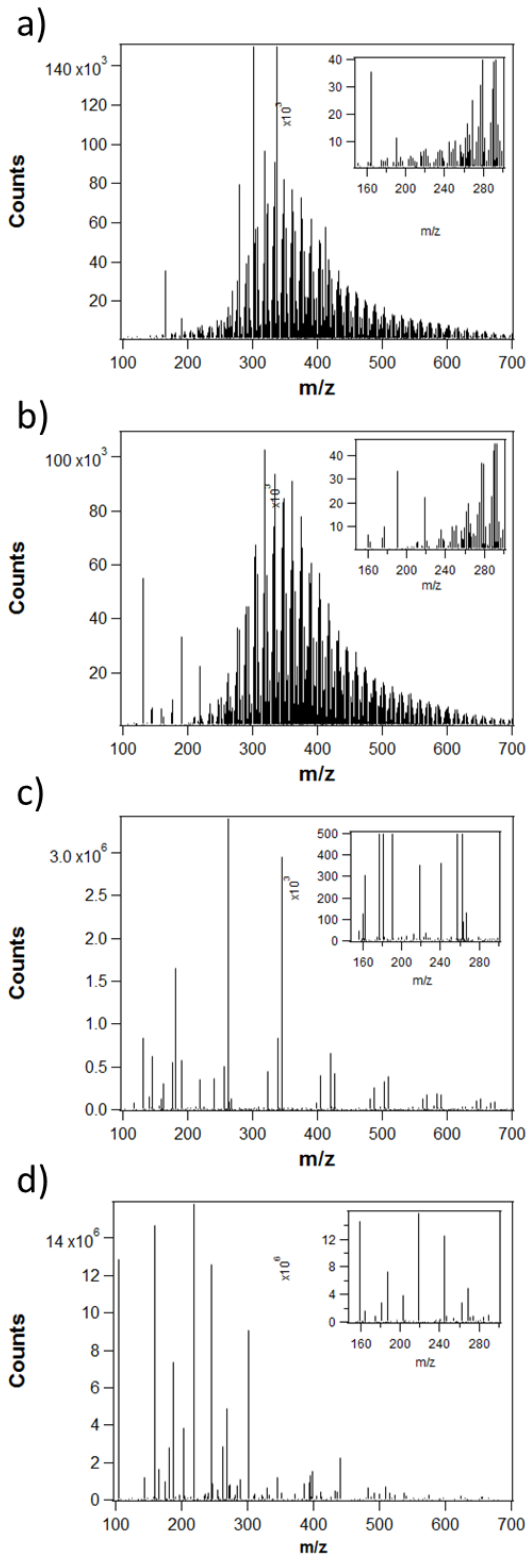

Figure S14. ESI-HRMS spectra of SRFA particle samples (a) before and after heating to (b) 150 °C, (c) 300 °C, and (d) 400 °C. Inlays are zoomed in spectra of the 150-300 m/z region.

Citations:

1. Pósfai, M.; Buseck, P. R., Nature and climate effects of individual tropospheric aerosol particles. *Annu. Rev. Earth Planet. Sci* **2010,** *38*, 17-43.
2. Fraund, M.; Pham, D. Q.; Bonanno, D.; Harder, T. H.; Wang, B.; Brito, J.; de Sa, S. S.; Carbone, S.; China, S.; Artaxo, P.; Martin, S. T.; Pohlker, C.; Andreae, M.; Laskin, A.; Gilles, M. K.; Moffet, R. C., Elemental mixing state of aerosol particles collected in central amazonia during GoAmazon2017/15. *Atmosphere* **2017,** *8* (9), 173.
3. Draxler, R. R.; D., R. G., HYSPLIT Model. NOAA ARL READY, 2012.
4. Jaitly; Mayampurath, A.; Littlefield, K.; Adkins, J. J.; Anderson, G. A.; Smith, R. D., Decon2LS: An open-source software package for automated processing and visualization of high resolution mass spectometry data. *BMC Bioinformatics* **2009,** *10* (87).
5. Roach, P. J.; Laskin, J.; Laskin, A., Higher-order mass defect analysis fo rmass spectra of complex organic mixtures. *Anal. Chem.* **2011,** *83* (12), 4924-4929.
6. Hopkins, R. J.; Tivanski, A. V.; Marten, B. D.; Gilles, M. K., Chemical bonding and structure of black carbon reference materials and individual carbonaceous atmospheric aerosols. *J. Aerosol Sci.* **2007,** *38*, 573-591.
7. Moffet, R. C.; Henn, T. R.; Tivanski, A. V.; Hopkins, R. J.; Desyaterik, Y.; Kilcoyne, A. L. D.; Tyliszczak, T.; Fast, J.; Barnard, J.; Shutthanandan, V.; Cliff, S. S.; Perry, K. D.; Laskin, A.; Gilles, M. K., Microscopic characterization of carbonaceous aerosol particle aging in the outflow from Mexico City. *Atmos. Chem. Phys.* **2010,** *10*, 961-976.
8. Moffet, R. C.; Tivanski, A. V.; Gilles, M. K., *Scanning x-ray transmission microscopy: applications in atmospheric microscopy. In Fundamentals and Applications in Aerosol Spectroscopy*. Taylor and Francis Books: New York, 2010.
9. Reid, J. P.; Bertram, A. K.; Topping, D.; Laskin, A.; Martin, S. T.; Petters, M. D.; Pope, F.; Rovelli, G., The viscosity of atmospherically relevant organic particles. *Nat. Commun.* **2018,** *956*, 1-14.
10. Song, M.; Liu, P. F.; Hanna, S. J.; Zaveri, R. A.; Potter, K.; You, Y.; Martin, S. T.; Bertram, A. K., Relative humidity-dependent viscosity of secondary organic material from toluene photo-oxidation and posible implications for organic particulate matter over megacities. *Atmos. Chem. Phys.* **2016,** *16*, 8817-8830.
11. Oja, V.; Suuberg, E. M., Vapor pressures and enthalpies of sublimation of d-glucose, d-xylose, cellobiose, and levoglucosan. *J. Chem. Eng. Data* **1999,** *44* (1), 26-29.
12. Kiyoura, R.; Kohei, U., Mechanism, kinetics, and equilibrium of thermal decomposition of ammonium sulfate. *Ind. Eng. Chem. Process Des. Develop.* **1970,** *9* (4), 489-494.
13. An, W. J.; Pathak, R. K.; Lee, B.-H.; Pandis, S. N., Aerosol volatility measurment using an improved thermodenuder: Application to secondary organic aerosol. *J. Aerosol Sci.* **2007,** *38*, 305-314.
14. Nie, W.; Hong, J.; Hame, S. A. K.; Ding, A.; Li, Y.; Yan, C.; Hao, L.; Mikkila, J.; Zheng, L.; Xie, Y.; Zhu, C.; Xu, Z.; Chi, X.; Huang, X.; Zhou, Y.; Lin, P.; Virtanen, A.; Worsnop, D. R.; Kulmala, M.; Ehn, M.; Yu, J. Z.; Kerminen, V. M.; Petaja, T., Volatility of mixed atmospheric humic-like substances and ammonium sulfate particles. *Atmos. Chem. Phys.* **2017,** *17*, 3659-3672.
15. Adachi, K.; Sedlacek, A. J.; Kleinman, L.; Chand, D.; Hubbe, J. M.; Buseck, P. R., Volume changes upon heating of aerosol particles from biomass burning using transmission electron microscopy. *Aerosol Sci. Technol.* **2017,** *52* (1), 46-56.
16. Haynes, W. M., *CRC Handbook of Chemistry and Physics*. 95th ed.; CRC Press, Taylor & Francis Group: Boca Raton, FL, 2014.
17. Cziczo, D. J.; Abbatt, J. P. D., Infrared observations of the response of NaCl, $MgCl_2$, NH_4HSO_4, and NH_4NO_3 aerosols to changes in relative humidity from 298 to 238 K. *J. Phys. Chem. A* **2000,** *104*, 2038-2047.

18. Foldvari, M., *Handbook of thermogravimetric system of minerals and its use in geological practice*. Geological Institute of Hundary: Budapest, 2011.
19. Zimm, B. H.; Mayer, J. E., Vapor pressures, heats of vaporization, and entropies of some alkali halides. *J. Chem. Phys.* **1944,** *12*, 362-369.
20. Grumback, M. P.; Martin, R. M., Phase diagram of carbon at high pressures and temperatures. *Phys. Rev. B* **1996,** *54* (22), 730-741.
21. Young, K. D.; LeBoeuf, E. J., Glass transition behavior in a peat humic acid and an aquatic fulvic acid. *Environ. Sci. Technol.* **2000,** *34*, 4549-4553.
22. Yu, J. Z.; Xu, J.; Yang, H., Charring characteristics of atmospheric organic particulate matter in thermal analysis. *Environ. Sci. Technol.* **2002,** *36*, 754-761.